1 # Precursor design for aerosol assisted plasma deposition of
2 poly(ethylene oxide)-like thin films: deposition mechanism and film
3 properties

4 Tijs Dekoster[a,b]; Rita Vos[b]; Karolien Jans[b]; Willem Van Roy[b]; Bernard Nisol[c]; Annelies Delabie[b,a]
5 a) KU Leuven, Kwantumchemie en Fysicochemie, Celestijnenlaan 200f, B3001 Leuven
6 b) imec, Kapeldreef 75, B3001 Leuven, Belgium
7 c) Molecular Plasma Group, Gaston Geenslaan 1, B3001 Leuven
8 Corresponding author details:
9 Annelies Delabie, imec, Kapeldreef 75, B3001 Leuven, Belgium. Email: annelies.delabie@imec.be

10 ## Abstract

11 Aerosol assisted plasma deposition using a cold atmospheric pressure plasma jet is promising for
12 deposition of poly(ethylene oxide)-like antifouling coatings. However, the impact of precursor volatility
13 and viscosity is currently not well understood. Decreasing the volatility by increasing the number of
14 ethylene oxide repeats in poly(ethylene glycol) dimethacrylate precursors improves the material
15 balance consistent with less precursor evaporation during transport and on the substrate. As more
16 and larger droplets reach the substrate this also influences the plasma polymerization. This does not
17 limit film formation from dimethacrylate precursors with nine ethylene glycol units resulting in stable
18 films with good antifouling properties. Better understanding of the mechanisms during aerosol-
19 assisted plasma deposition will facilitate design of adequate precursors for deposition of
20 multifunctional coatings.

Introduction

Cold atmospheric plasma jets (CAPjets) have received a lot of attention in recent years because of their low equipment cost, potential for mass manufacturing and ability to treat temperature-sensitive substrates and deposit functional films from temperature sensitive precursors [1]. Thanks to these advantages, CAPjets have found applications in a wide variety of fields, such as adhesion improvement in automotive industry [2], barrier coatings for food packaging [3], hydrophobic coatings for textile treatment [4] and anti-icing [5]. A continued challenge in life-science industry is the deposition of antifouling coatings in a scalable, mass-manufacturable way. Antifouling coatings prevent the binding of proteins and cells to the device surface, which often hampers the sensitivity and limits the lifetime of biosensors and lab-on-chip devices. A common strategy to prevent biofouling is to use poly(ethylene oxide) (PEO) layers, which are considered as the "gold standard" for anti-fouling layers [6]. Several approaches for surface modification with PEO exist. They can be grouped in wet chemical methods such as self-assembled monolayers [7], [8], [9], grafted polymer brushes [10], [11], [12], [13], UV-polymerization [14], [15] and dry methods such as plasma deposition at low pressure [16], [17] and atmospheric pressure [18], [19].

The precursors used for plasma deposition of PEO, such as tri(ethylene glycol) dimethyl ether and tetra(ethylene glycol) dimethyl ether, typically have a low vapor pressure (2.6 Pa and <1.33 Pa at 20 °C, respectively), which makes them impractical to use for vapor phase deposition at atmospheric pressure. (Except when noted otherwise all vapor pressures in this work are quoted from [20]). Aerosol-assisted plasma deposition alleviates the need for highly volatile precursors. Consequently, aerosol injection may facilitate the utilization of precursors with many ethylene oxide repeats, potentially increasing the ethylene oxide content in the coating to improve the antifouling properties. In recent years, numerous studies appeared on aerosol assisted plasma deposition of organic coatings at atmospheric pressure from precursors with a broad range of vapor pressures. Examples of used precursors and their vapor pressure are acrylic acid (533 Pa) [21], hydroxyethyl methacrylate (8 Pa) [22] and dodecyl acrylate [23]. To obtain stable coatings with the appropriate functionality, a soft plasma polymerization is desired. During soft plasma polymerization the reactive sites of the precursor are activated while the functionality e.g. the ethylene oxide unit is preserved. This has been shown for several acrylate and methacrylate precursors, for deposition from both aerosol [23], [24] and vapor phase [25]. An important parameter to achieve a soft-plasma polymerization from precursors in the vapor phase is the energy-per-molecule available, which depends on the ratio of the plasma power and the precursor flow [26]. Also for plasma polymerization from the liquid phase the dependence on the energy-per-molecule ratio has been observed [24], [25], [27], for example the parameter has been

1 shown to relate to the cross-linking and hardness of coatings from hexanediol dimethacrylate
2 precursors using aerosol assisted plasma deposition [24].
3 However, the complexity of the deposition process increases when using aerosols. The precursor vapor
4 pressure can strongly affect droplet evaporation during the transport process and thus the state (liquid
5 or vapor) in which the precursor reaches the substrate Also, the precursor viscosity could affect the
6 aerosol droplet size as well as droplet spreading on the substrate. It has been observed that precursors
7 with a low vapor pressure can result in thicker coatings as droplet evaporation slows down [28]. The
8 resulting films show droplet-like morphology, indicating that the precursor reaches the substrate as a
9 liquid. Furthermore, the interaction between the plasma and the liquid is highly complex, with
10 penetration depths varying based on the active species involved. For thicker liquid layers the plasma
11 potentially interacts only with a limited part of the liquid layer [29].
12 Therefore, it is important to understand the effect of precursor vapor pressure and viscosity during
13 aerosol assisted plasma deposition. In this paper, we investigate atmospheric pressure plasma
14 deposition of PEO using precursors with methacrylate terminations and a varying number of ethylene
15 oxide repeating units to tune their vapor pressure and viscosity. The precursors have a low vapor
16 pressure and cannot easily be used for vapor phase deposition, but they can be used during deposition
17 with a CAPjet. Unsaturated bonds such as the C=C bonds from the methacrylate groups could be
18 preferentially activated in a plasma, potentially preserving the ethylene oxide part of the precursor
19 [30], [31] and allowing for a soft-plasma polymerization [27]. First, we discuss the different processes
20 that can occur during aerosol assisted plasma deposition. Next, we calculate the material balance
21 defined as the ratio between the deposited mass and the consumed precursor mass. We also study
22 the impact of the physical precursor properties on the film growth and the chemical composition, the
23 stability and antifouling properties using various complementary techniques such as atomic force
24 microscopy (AFM), scanning electron microscopy (SEM), Fourier-Transform Infrared spectroscopy (FT-
25 IR) and X-ray photoelectron spectroscopy (XPS).
26

27 ## Materials and methods

28 ### Chemicals

29 Ethylene glycol dimethacrylate (EGDMA), di(ethylene glycol) dimethacrylate (2EGDMA), tri(ethylene
30 glycol) dimethacrylate (3EGDMA), poly(ethylene glycol) dimethacrylate (PEGDMA) Mn 550 g/mol
31 corresponding to 9 ethylene oxide repeats on average, acetic acid, toluene and goat anti-mouse IgG
32 antibody labelled with Atto647N fluorescent dye were purchased from Sigma Aldrich,
33 3-[methoxy(polyethyleneoxy)6-9] propyltrimethoxysilane was purchased from Gelest and 11-
34 azidoundecyltrimethoxysilane was purchased from abcr GmbH. The structure of the used precursors

1 can be found in Supplementary figure 5. Acetone and isopropanol were purchased from CMC
2 materials. The precursor boiling points [32], vapor pressure and viscosity can be found in Table 1. The
3 viscosity was measured with a Brookfield Analis cone Plate viscosity meter at 25 °C.
4

1 *Table 1: Physical precursor properties. *The vapor pressures are estimated based on the boiling points*
2 *found at the product information of Sigma Aldrich [20] and the Clausius Clapeyron equation [33] using*
3 *an enthalpy of vaporization (ΔH_{vap}) of 50 kJ/mol, the value for EGDMA [34]. Values of ΔH_{vap} for the*
4 *other compounds were unavailable, but for homologous series of molecules ΔH_{vap} typically increases*
5 *with increasing molecular weight [35] hence the estimations for 2EGDMA and 3EGDMA are upper*
6 *bounds.*

	EGDMA	2EGDMA	3EGDMA	PEGDMA
Boiling point (°C) [20]	98 at 700 Pa	134 at 300 Pa	170 at 700 Pa	/
Estimated vapor pressure (Pa) at 25 °C*	12.5	< 1.2	< 0.9	/
Vapor pressure (Pa) [20]	13.3 @21°C	/	/	/
Viscosity (mm2/s) at 25 °C	3.0	5.7	8.6	42.4
Density (g/cm^3) [20]	1.05	1.08	1.09	1.10

7
8 ## Substrates
9 P-type silicon wafers with (001) crystal orientation (purchased from MEMC Electronic Materials) were
10 precleaned using a two-step cleaning sequence with an O_3 based step for oxidation and diluted HF for
11 subsequent oxide removal [36]. A clean chemical oxide was regrown using ozonated deionized water
12 (DIW) in the final rinsing step. The wafers were then cleaved into 3 cm x 3 cm coupons. Particles
13 generated during cleaving were removed by subsequent sonication in acetone and isopropanol for 10
14 minutes. Immediately before plasma deposition, the substrates received an additional 15 min UV/O_3
15 clean (UVO-cleaner, Jelight Company Inc.) to remove any airborne organic contamination. Silicon
16 coupons with a 100 nm thermal oxide were used for antifouling measurements and cell adhesion
17 testing.
18 ## Plasma deposition
19 All atmospheric pressure plasma depositions (APPD) were performed using the PlasmaSpot®
20 (Molecular Plasma Group (MPG), Luxembourg) dielectric barrier discharge (DBD) plasma jet [36]. This
21 R&D system enables the generation of atmospheric pressure cold (near ambient temperature)
22 plasmas. It consists of two concentric tubular electrodes (Figure 1a). The external one is covered with
23 a dielectric layer and is connected to the power source, while the inner one is grounded. The
24 PlasmaSpot® powered electrode was fed with a high-voltage of up to 15 kV peak-to-peak, at a
25 frequency in the 40-50 kHz range. The nominal power output was 150 W for all experiments. A fixed
26 flow rate of 80 standard liters per minute (slm) argon (Alphagaz, Airliquide) was fed to the system
27 between the concentric electrodes, acting as discharge gas.

The precursor was supplied to the plasma inside the hollow inner electrode in the form of an aerosol, generated by an MPG atomizer (Figure 1c). The exact working principle of the atomizer is described elsewhere [36]. In brief, a primary argon gas flow (atomizer gas flow) accelerates through a circular orifice (size 0.4 mm), generating an underpressure which draws up liquid from the precursor bottle through the Venturi effect. The liquid is "atomized" or aerosolized by the high gas velocity. The atomizer gas flow was varied between 0.75 and 1.05 slm. The corresponding precursor mass flows for the different precursors were measured by weighing the precursor bottle before and after deposition and can be found in Figure 3a. After atomization the aerosols were diluted using a fixed argon dilution flow of 5 slm and supplied to the plasmahead with silicone tubing of 45 cm length and an inner diameter of 3.5 mm.

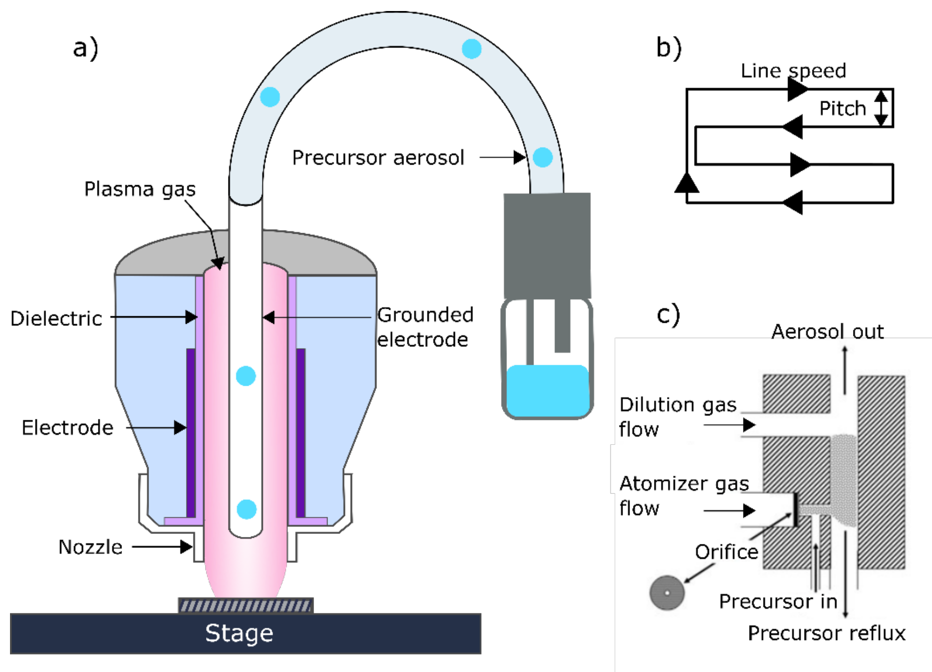

Figure 1: Schematic of the a) plasma jet used for the experiments. b) scanning motion of the plasma jet. c) atomizer for aerosol generation.

To shield the reaction area from air, a 3D-printed ring-shaped nozzle from acrylonitrile butadiene styrene with a diameter of 25 mm was attached to the PlasmaSpot®, resulting in a line width of 25 mm. In this nozzle the plasma afterglow is combined with the precursor. The nozzle to substrate distance was fixed at 2 mm.

Plasma deposition was performed across the entire sample surface by scanning in a serpentine pattern with a 16 mm/s line speed and a pitch of 2 mm between the lines (Figure 1b). This means that in one scan the nozzle passes ~12 times over each location. All films for chemical characterization were deposited with 2 scans of the plasma jet. Thin films for analysis of the film growth were deposited with

1 scan of the plasma jet at a line speed of 100 mm/s and a pitch of 8 mm. For certain films, the temperature of the substrate was controlled by mounting the sample on a hotplate. Three temperatures were tested: 30°C, 60°C and 90°C. The indicated temperatures are the temperature of the hotplate and do not compensate for potential cooling or heating of the substrate by the plasma gas.

Aerosol characterization

The aerosol droplet size distribution was measured with a Palas promo LED 2000 scattered-light aerosol spectrometer. The measured size range was 0.1 to 10 µm. The atomizer was connected directly to the spectrometer with a silicone tubing with a length of 45 cm and an inner diameter of 3.5 mm. The maximum detectable particle density of the spectrometer is $10^6/cm^3$. The atomizer gas flow used for the measurements was set at 0.7 slm to avoid saturation of the detector.

Film characterization

Fourier-Transform Infrared spectroscopy (FT-IR) was performed in transmission mode using a Nicolet 6700 system from Thermofisher. 60 scans per sample were performed from 400 cm^{-1} to 4000 cm^{-1} with a resolution of 4 cm^{-1}. The background was corrected by subtracting the spectrum of a blank silicon coupon, obtained right before the measurements. TQ-analyst (Thermofisher) software was used to obtain the integrated area of the vibration bands, enabling quantitative analysis. The stability of the films in water was determined by comparing the area of the integrated band containing the symmetric and asymmetric CH_2, and CH_3 stretch before and after soaking 10 minutes in deionized water.

The composition of the deposited films was further analyzed by XPS measurements using a QUANTES instrument from Physical electronics. The measurements were performed using a monochromatic photon beam (Al Kα: hv = 1486.6 eV), the pass energy was 69 eV and the step size 0.125 eV. Charge compensation was used. Note that the exact quantification of the components of the C 1s peak is dependent on the chosen fitting parameters. The background was corrected using a Shirley model [37].

The film thickness was determined using a DEKTAK XT profilometer from Bruker, by scanning from a part of the sample masked during deposition to the polymer film, using a stylus with a 2 µm tip radius, a force setting of 1 mg to avoid scratching of the coating and a scan speed of 50 µm/s. To assess the validity of using a profilometer, the thickness of 4 reference samples was compared with the thickness determined via SEM images (Supplementary figure 9). The measured values are in relatively good agreement given the large uncertainty on a thickness determination with SEM.

AFM characterization was performed with a Bruker Dimension Edge AFM in standard tapping mode. OMCL-AC160TS-R3 AFM tips (Olympus) with a resonant frequency of 300 kHz were used. An area of

1 100x100 µm^2 was scanned with 128 lines and 128 points per line at a scan rate of 100 µm/s. Shown
2 data originates from the forward height channel. Data processing was performed with NanoScope
3 Analysis software (Bruker) and a 3rd order plane subtraction was done to correct the data.
4 SEM images ware taken with a Verios G4 XHR SEM from Thermofisher. Before SEM analysis the films
5 were coated with 0.5 nm Pt.
6 Optical microscopy images were taken with a Zeiss LSM 780 confocal microscope. The diameter
7 distribution of the rings was measured using ImageJ image processing software. Only non-overlapping
8 rings were considered.
9 To determine the material balance, the mass of films deposited with 4 scans at 0.9 slm atomizer gas
10 flow was determined by weighing the silicon substrate before and after deposition. Silicon substrates
11 with an area of approximately 10x10 cm^2 were used to have sufficient mass for an accurate
12 measurement and to prevent precursor landing next to the substrate. The mass of the films was
13 determined by weighing the mass of the samples before and after deposition. A CPA225D
14 microbalance from Sartorius was used with an error of 0.01 mg. The mass of the coatings varied
15 between 2 and 7 mg.

16 ## Antifouling

17 Antifouling tests were performed with PEO-like films deposited in on SiO_2 substrates with 100 nm
18 thermal oxide. Two passes of deposition were used, with a precursor gas flow of 0.75 slm and a plasma
19 power of 150 W. After film deposition, the samples were soaked for one hour in deionized water and
20 blown dry with nitrogen to remove any non-crosslinked material. As controls, SiO_2 substrates with 100
21 nm thermal oxide either non-coated or coated with a
22 3-[methoxy(polyethyleneoxy)6-9]propyltrimethoxysilane (PEO-SAM) or an
23 11-azidoundecyltrimethoxysilane (Azide-SAM). For PEO-SAM deposition, the samples were
24 submerged in a solution containing 0.5 v-% of
25 3-[methoxy(polyethyleneoxy)6-9]propyltrimethoxysilane, 0.08 v-% acetic acid in toluene for 12 hours,
26 followed by sonication in acetone and isopropanol. For azide-SAM deposition, the samples were
27 loaded into a home-built stainless-steel vacuum chamber as described in [39]. The deposition time
28 was two hours, using 120 µL of 11-azidoundecyltrimethoxysilane at 145°C at a pressure of 25 mbar.
29 The antifouling properties were quantified using fluorescence microscopy (Zeiss LSM 780 confocal
30 microscope). The samples were subsequently incubated for 30 minutes with 5 µL droplets of an
31 antibody solution (200 µg/mL anti-mouse IgG antibody labelled with a Atto647N fluorescent dye in
32 150 mM phosphate buffered saline (PBS) PH 7.4). After incubation the samples were thoroughly
33 washed with PBS buffer and DIW to remove all salt residues before inspection with the microscope.

Results and discussion

Processes during aerosol assisted plasma deposition

To understand film formation during aerosol assisted plasma deposition and the material balance, it is necessary to consider all main processes that take place.

The processes that lead to film formation at and near the substrate and in the plasma head and nozzle are summarized in Figure 2. The starting point is the formation of a precursor aerosol by the atomizer. An inert gas is used to transport the aerosol from the atomizer through the plasma head and nozzle to the substrate. During transport, the size distribution and number density of the droplets could change due to evaporation (1 in Figure 2)[40], which was observed before in the context of aerosol assisted plasma deposition [28]. We will estimate droplet evaporation for liquids with different vapor pressures later in this work. In addition, reactions and polymerization through interactions with the plasma in the nozzle may create sideproducts (2 in Figure 2). Thus, the gas flow that passes through the nozzle may contain gas phase species in addition to the aerosol.

Processes at and near the substrate include the impact and spreading of droplets on the substrate, adsorption of gas phase species on the substrate, interactions with plasma, chemical reactions and polymerization, evaporation and desorption of volatile reaction products. The collection efficiency by the substrate is defined as the fraction of droplets of a certain diameter that is collected on the substrate. It depends on the droplet size and as such the droplet size distribution can affect the material balance [41]. Large droplets have high inertia and may maintain their direction when the gas stream impinges on the substrate. They will impact and spread out and possibly evaporate on the substrate (3 and 6 in Figure 2) [41] while reactions and polymerization occur by interactions with the plasma, resulting in film formation (4 in Figure 2). Small droplets have a higher probability to follow the gas stream to the exhaust and therefore have lower probability to impact on the substrate (5 in Figure 2)[41]. Thus, for precursors with a low vapor pressure mainly liquid precursor is expected to be present on the substrate after impact and spreading, and reactions with the plasma result in polymerization and film formation (4 Figure 2). Since there is no electrical field between the plasma and the substrate, field driven migration of charged droplets as observed e.g. in low-pressure plasma deposition [42] does not play a role. Therefore, droplet transport to the substrate is most likely driven by advective and inertial forces. Volatile reaction products can be generated, that desorb and are removed to the exhaust (8 in Figure 2). Growth contributions could come from reactions of adsorbed gas phase molecules (7 in Figure 2). Finally, volatile reaction products and vapor phase precursor are removed from the reaction area (8 in Figure 2).

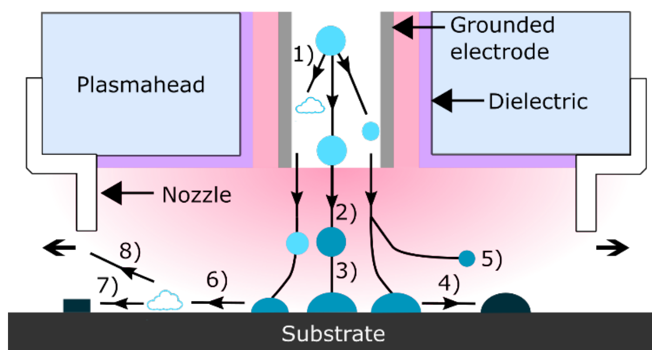

Figure 2: Overview of precursor transport and film formation during aerosol assisted plasma deposition. 1) Evaporation, ripening and coalescence of droplets during transport, turning large droplets into small droplets and gas phase species. 2) Reactions/polymerization during transport. 3) Large droplets impact on substrate. 4) Reactions/polymerization after impaction. 5) Small droplets do not impact substrate. 6) Evaporation and desorption after impaction. 7) Reactions/polymerization of vapor phase precursor. 8) Removal of vapor phase precursor from the reaction area.

Impact of methacrylate precursor physical properties on APPD process

To investigate the impact of the physical precursor properties like volatility and viscosity on the film growth and material balance, we compare deposition from precursors with a varying number of ethylene oxide repeats in between two methacrylate end groups. The precursor viscosity increases with the number of ethylene oxide repeats in the precursor, while vapor pressure decreases (Table 1) [32]. The deposition process consists of 3 main steps: aerosol generation in the atomizer, transport of the aerosol droplets to the substrate and deposition of droplets and vapor on the substrate.

Injected precursor mass flow and aerosol droplet size

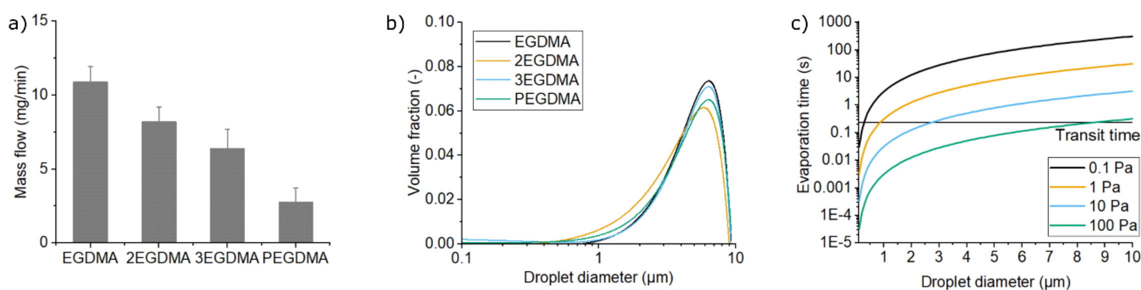

Figure 3: a) Precursor mass flow at 0.9 slm atomizer gas flow, determined by weighing the precursor bottle before and after deposition. b) Plot of the normalized distribution of the aerosol droplet size weighted by the aerosol volume. c) Estimated droplet evaporation time calculated with eq. 4 as a function of the droplet diameter, for liquids with a vapor pressure of 0.1, 1, 10 and 100 Pa, and with gas phase diffusion coefficient calculated according to [43] using the material parameters of EGDMA. Horizontal line: travel time from the atomizer to the substrate.

First, we discuss the aerosol generation by the Collison-type atomizer. The primary parameter controlling the rate of aerosol formation and precursor mass flow is the atomizer gas flow (Figure 1c). This gas flow accelerates through a 0.4 mm orifice creating an underpressure that aspirates liquid into the atomizer and breaks the liquid up into droplets. There is a self-regulating mechanism in the aspiration of the liquid into the atomizer [44], and a built-in size selection mechanism limiting the maximum droplet size that can escape [47]. The combination of these processes typically leads to a decrease in output aerosol density with increasing liquid viscosity [44].

For a constant atomizer gas flow at 0.9 slm, we determine the precursor mass flow by weighing the precursor bottle before and after deposition. The precursor mass flow decreases with the number of ethylene oxide repeats and increasing liquid viscosity of the precursor (Figure 3a). Next we measure the aerosol size distributions for the different precursors and we find that all precursors have similar aerosol droplet size distributions (Figure 3b, raw data Supplementary figure 1). The volume median droplet diameter (defined by the tool manufacturer as the diameter which divides the volume of the aerosol into two equal halves) is approximately 5 µm for all precursors (Supplementary table 1). These observations are consistent with the working mechanism of the Collison-type atomizer [44], [45].

Second, we discuss the transport of droplets to the substrate. To understand the influence of precursor vapor pressure on aerosol evaporation during transport we estimate the droplet evaporation time τ_{evap} for liquids with varying vapor pressure. Droplet evaporation is a complex process [40], [46], [47] and a detailed analysis is beyond the scope of the present paper. Here a first-order estimation is given based on the Maxwell evaporation model for droplets [47], [48]

$$\frac{dm}{dt} = -\frac{4\pi rDM}{RT}\left(p_{v,s} - p_{v,\infty}\right) \quad (1)$$

which assumes that mass transport in the gas phase away from the droplet is purely diffusive. Here m the droplet mass, r the droplet radius, D the diffusion coefficient of the vapor (of the droplet material) in the surrouding gas, $p_{v,s}$ and $p_{v,\infty}$ the partial pressure (of the droplet material) in the surrounding gas at the surface of the droplet and at an arbitrarily large distance respectively, M the molar mass, R the universal gas constant and T the temperature. Under the further simplifying assumption of isothermal evaporation and assuming no vapor in the carrier gas ($p_{v,\infty} = 0$), and with

$$m = \frac{4}{3}\pi r^3 \rho \quad (2)$$

with ρ the density of the droplet, eq. 1 becomes

$$\frac{4}{3}\pi\rho\frac{dr^3}{dt} = -\frac{4\pi rDM}{RT}p_{v,s} \quad (3)$$

This can be integrated to [47], [48]

$$r^2(t) = r^2(t_0) - \frac{2DM}{\rho RT}p_{v,s}\,(t - t_0) \quad (4)$$

This gives us an analytical expression to estimate the impact of vapor pressure on the evaporation time of the droplets. An estimation of the droplet evaporation time τ_{evap} can be obtained from the time t

1 at which $r(t) = 0$. The calculation is performed for three relevant vapor pressures, as the exact vapor
2 pressure of the precursors is not known: 0.1, 1, 10 and 100 Pa. The evaporation time of a 1 µm
3 diameter droplet strongly decreases from 3.2 s to 3.2 ms for an increase in vapor pressure of 0.1 to
4 100 Pa (Figure 3c). When comparing τ_{evap} with the transit time (0.237 s, estimated by dividing the
5 cross-section of the silicone tubing by the gas flow rate and the tube length) of a droplet from the
6 atomizer to the substrate, the smallest droplets evaporate completely before reaching the substrate.
7 The minimal droplet sizes to survive are 0.3, 0.9, 2.7 and 8.5 µm for a vapor pressure of 0.1, 1, 10 and
8 100 Pa respectively. This means that for the range of vapor pressures presented here, the largest
9 droplets will never fully evaporate. In the next section we will investigate the final step in the
10 deposition process: the deposition of droplets and vapor on the substrate.

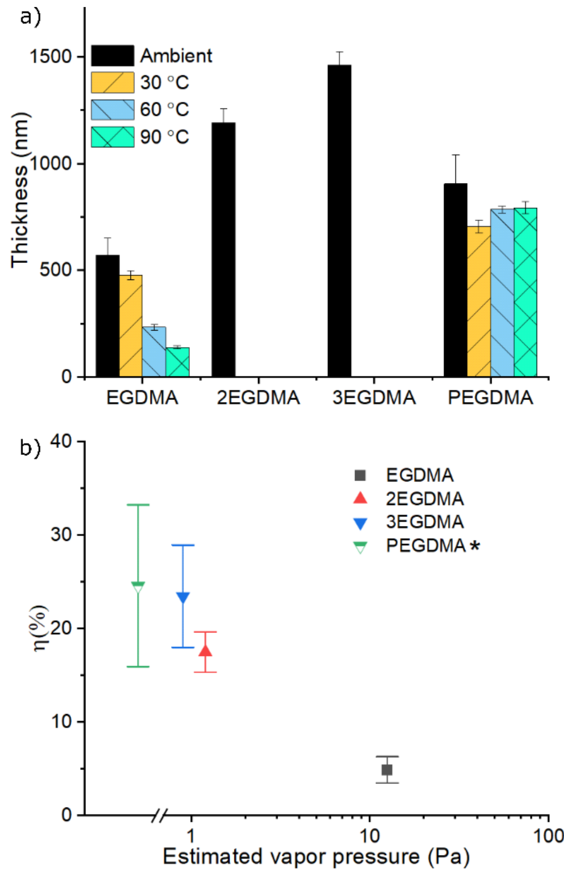

*Figure 4: Film thickness determined by profilometry, for films deposited at 0.9 slm atomizer gas flow, 2 scans and different substate temperatures. b) Material balance η for films deposited at 0.9 slm atomizer gas flow 4 scans and ambient substrate temperature. *Vapor pressure of PEGDMA unknown. The error bars represent the standard deviation on 3 separately deposited samples.*

Film thickness and material balance

To analyze film growth for the different precursors, we determine the film thickness for films deposited in the same conditions, i.e. at ambient substrate temperature using a 0.9 slm atomizer gas flow. For EGDMA, 2EGDMA and 3EGDMA, the film thickness strongly increases with increasing number of ethylene oxide repeats in the precursor (Figure 4a), despite the decreasing precursor mass flow (10.9, 8.2 and 5.9 mg/min for EGDMA, 2EGDMA and 3EGDMA respectively, Figure 3a). In contrast, for 3EGDMA and PEGDMA, the film thickness decreases with increasing number of ethylene oxide repeats in the precursor (Figure 4a), consistent with decreasing precursor mass flow (5.9 and 2.3 mg/min for 3EGDMA and PEGDMA respectively, Figure 3a).

The material balance

$$\eta = \frac{Mass\ of\ deposited\ material}{Mass\ of\ injected\ precursor} \qquad (5)$$

indicates which fraction of the mass leaving the atomizer is ultimately deposited on the substrate.

1 We find that η strongly increases with increasing number of ethylene oxide repeats in the precursor
2 from EGDMA to PEGDMA, thus with decreasing precursor volatility (Figure 4b, Table 2).
3 We discuss the different steps in the deposition process to understand the differences in material
4 balance. Factors that can affect η are differences in aerosol size distribution, precursor evaporation
5 during transport and evaporation after impaction, processes 1, 5 and 6 in Figure 2. First, the size
6 distribution of the droplets leaving the atomizer is very similar for all precursors (Figure 3b), as such
7 this does not explain the differences in material balance. Second, precursors with higher vapor
8 pressure evaporate more during transport, resulting in smaller droplet sizes and/or a decreased
9 number density of droplets (Figure 3c). This can decrease η by a twofold effect, i.e. precursor in the
10 vapor phase contributes less to film formation due to the short residence time in the nozzle and the
11 aerosol collection by the substrate is lower for small droplets [41]. To estimate the effect of the droplet
12 size on the collection efficiency, a fluid dynamics simulation is performed (Supplementary information
13 section 7). The collection efficiency decreases when the size of the droplets decreases: from ~100%
14 for 10 µm diameter droplets to <50% for droplets with a diameter smaller than 2.5 µm (Supplementary
15 figure 8), in agreement with literature [41]. Precursor evaporation during transport has been
16 previously observed [28], and it can account for the increase in η as the precursor vapor pressure
17 decreases. Third, to assess the importance of evaporation after impaction, the impact of substrate
18 heating is investigated. As expected, increasing the substrate temperature from room temperature to
19 90°C during deposition with the most volatile precursor (vapor pressure 12.5 Pa at 25°C) results in a
20 strong decrease of film thickness (570 nm at room temperature versus 140 nm at T_{sub} = 90 °C). On the
21 other hand, there is no significant influence of the substate temperature on deposition with the less
22 volatile PEGDMA precursor (Vapor pressure < 0.9 Pa at 25°C) (Figure 4a). This indicates that
23 evaporation after impaction affects the film thickness only for precursors with a high volatility. One
24 final explanation is the lower precursor mass flow while the plasma conditions are constant, which
25 could increase the effective interaction of the plasma with the precursor.
26
27 *Table 2: Deposited mass, deposition rate, material balance η and density for films deposited with 4*
28 *scans at 0.9 slm atomizer gas flow. The error bars represent the standard deviation on 3 separately*
29 *deposited samples.*
30

	EGDMA	2EGDMA	3EGDMA	PEGDMA
Deposited mass (mg)	2.5 ± 0.5	6.7 ± 0.1	7.1 ± 0.2	3.2 ± 0.1
Deposition rate (mg/min)	0.53 ± 0.1	1.43 ± 0.01	1.50 ± 0.05	0.68 ± 0.01
η (%)	5 ± 1	17 ± 2	23 ± 5	25 ± 8
Density (g/cm³)	1.10 ± 0.08	1.33 ± 0.06	1.16 ± 0.04	1.29 ± 0.11

1 *Impact of precursor properties on coating morphology*

2 To investigate the deposition mechanism during the initial stages of film growth and the impact of the
3 precursor properties, a morphological analysis by AFM after deposition with short deposition time (1
4 scan, 100 mm/s scan speed, pitch 8 mm) is performed. Ring-shaped features with diameters between
5 20 and 55 µm are observed for deposition with all precursors (Figure 5). The maximum height of the
6 features increases with increasing number of ethylene oxide repeats in the precursor, from 20 nm for
7 EGDMA to 130 nm for PEGDMA. The ring features confirm that individual droplets in the liquid phase
8 impact the substrate and spread out over the surface, as observed for other precursors with a low
9 vapor pressure [28], [49], and in agreement with our droplet evaporation time estimation (Figure 3b).
10 The more prominent rings formed for EGDMA (as compared to PEGDMA) can indicate that evaporation
11 occurs after impaction for this more volatile precursor [49], consistent with the strong effect of
12 substrate temperature on film thickness for EGDMA (figure 3b). The average width of the rim of the
13 ring slightly increases with increasing number of ethylene oxide repeats in the precursor, from 2.8 for
14 EGDMA to 4.4 µm for 3EGDMA (Supplementary figure 2). For PEGDMA the width of the ring increases
15 further, resulting in an almost completely closed feature, as indicated by the line scans in Figure 5.
16 Optical microscopy images (Figure 6 a-d) are used to determine the diameter of the rings encountered
17 in the early deposition stages, to have a large enough field of view for a statistically relevant
18 information. As before, films were deposited with 1 scan at 100 mm/s to be able to observe individual
19 droplets on the substrate. The average diameter of the features is decreasing from 53 µm for EGDMA
20 to 24 µm for PEGDMA, and the distribution becomes more narrow (Figure 6e) with increasing number
21 of ethylene oxide repeats in the precursor. The diameter of the rings is much larger than the volume
22 median droplet diameter for depositions with all precursors (~5µm, respectively, Figure 3b). This
23 indicates that the droplets spread out on the substrate, which increases their surface-to-volume ratio.
24 To quantify the difference in spreading for the different precursors, the spreading ratio S is calculated
25 as:

26 $$S = \frac{D_{ring}}{D_{droplet}} \quad (6)$$

27 S quantifies how much a droplet spreads out when impacting on a substrate, with D_{ring} the diameter
28 of the ring, and

29 $$D_{droplet} = \left(\frac{6}{\pi} V_{ring}\right)^{\frac{1}{3}} \quad (7)$$

30 the diameter of a droplet of volume V_{ring}. The volume of the ring feature is obtained from the AFM
31 images by integration of the line scans:

32 $$V_{ring} = \int 2\pi r h dr \quad (8)$$

33 with r the distance from the center of the ring and h the height of the ring. Here, it is assumed that
34 the volume is maintained during impaction, and potential volume changes due to evaporation and

1 chemical reactions are ignored at this point. The droplet diameter calculated from the ring volume is
2 shown in Figure 7a. There are no large differences between the droplet diameters for the different
3 precursors. This is consistent with the measured aerosol size distributions, which were found to be
4 very similar for all precursors (Figure 3c).
5 S decreases with increasing number of ethylene oxide repeats in the precursor, from S = 18 for EGDMA
6 to S = 7 for PEGDMA (Figure 7b). The same trend is also seen in the average diameter of the features,
7 which is smaller for PEGDMA as compared to EGDMA (Figure 6e), and their increased height as
8 observed from AFM (Figure 5). This observation is in agreement with research on droplet spreading
9 for inkjet printing which has demonstrated that the amount of spreading of droplets impacting on a
10 substrate is inversely proportional to the viscosity of the precursor, for liquids with similar surface
11 tension [50]. Surface tension can also affect the droplet spreading [50]. Therefore, we attempted to
12 measure the contact angle of the precursors on silicon, but for all precursors the contact angle was too
13 small to be measured. The increased spreading for precursors with a lower viscosity could lead to more
14 efficient activation by the plasma. Plasma-liquid interactions are highly complex, and the penetration
15 depth of the active species may highly depend on the plasma setup and the type of active species
16 (ions, electrons, radicals) [51], [52].
17 Finally, we investigate the morphology of closed films deposited with 2 scans, 16 mm/s scan speed and
18 pitch of 2 mm (Figure 8a-d), resulting in a much longer deposition time compared to the films in the
19 early deposition stage (Figure 5). All films have an irregular surface with macroroughness. The surface
20 morphology of films from EGDMA, 2EGDMA and 3EGDMA is comparable, with some of the ring
21 features still being visible. The root mean squared (RMS) roughness of the coatings increases from 38
22 nm for EGDMA to 78 nm for 3EGDMA (Table 3), which can potentially be explained by the increase in
23 thickness from 388 to 836 nm. The RMS roughness slightly decreases for PEGDMA to 64 nm. SEM
24 imaging also confirms that the films have an irregular morphology with macroroughness (Figure 8e-g).
25

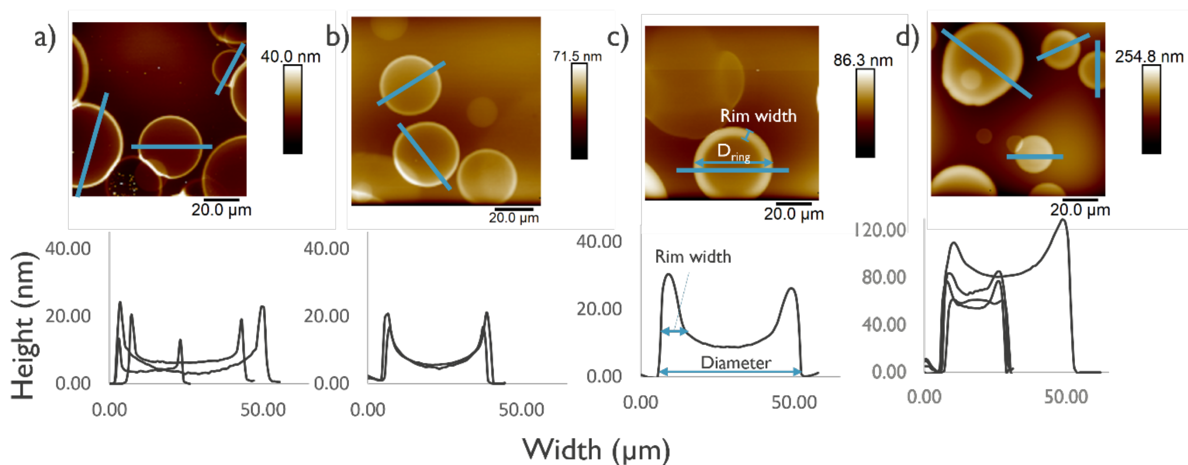

26

Figure 5: AFM images with line profiles of typical ring features for a) EGDMA, b) 2EGDMA, c) 3EGDMA, d) PEGDMA, deposited at an atomizer gas flow 0.75 slm, 1 scan, 100 mm/s scan speed and pitch of 8mm. Blue lines indicate line profiles plotted below.

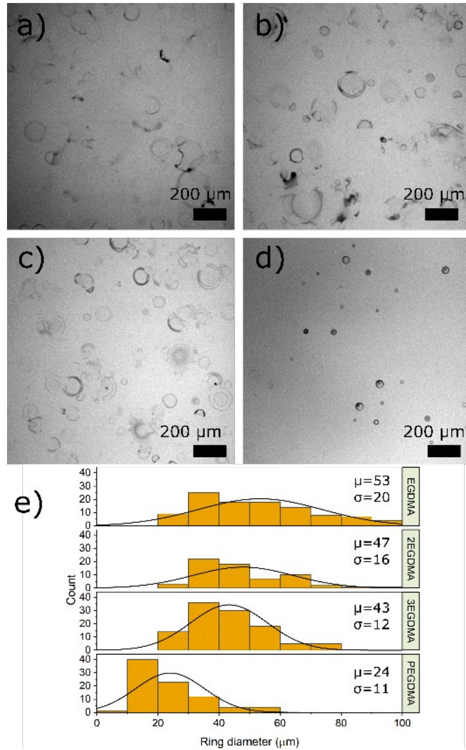

Figure 6: Optical microscopy images of films deposited at an atomizer gas flow 0.75 slm, 1 scan, 100 mm/s scan speed and pitch of 8mm: a) EGDMA b) 2EGDMA c) 3EGDMA d) PEGDMA. e) Histogram of the diameter distribution of the ring features (65< datapoints per precursor), fitted with a normal distribution (μ=mean, σ=standard deviation).

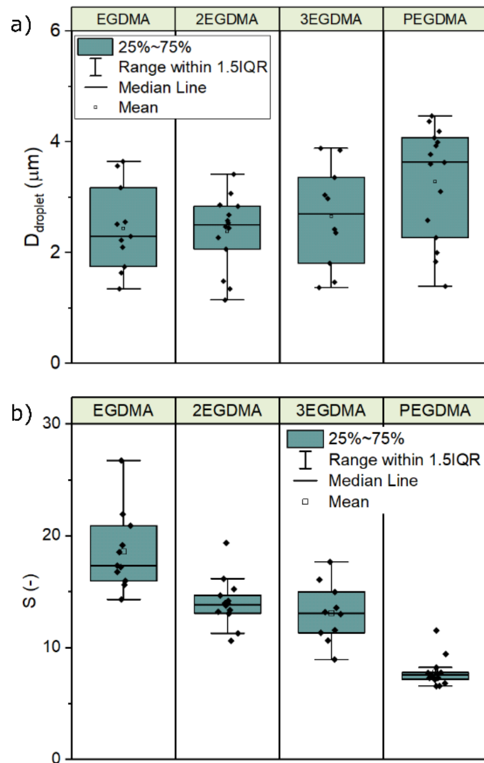

1

2 *Figure 7: a) Box plots of the diameter of a droplet with the same volume as the rings from Figure 5,*
3 *calculated with equation 6. b) Box plots of the spreading ratio S, for films deposited at an atomizer gas*
4 *flow 0.75 slm, 1 scan, 100 mm/s scan speed and pitch of 8mm. Based on 15 datapoints per precursor.*
5 *IQR= interquartile range.*

6 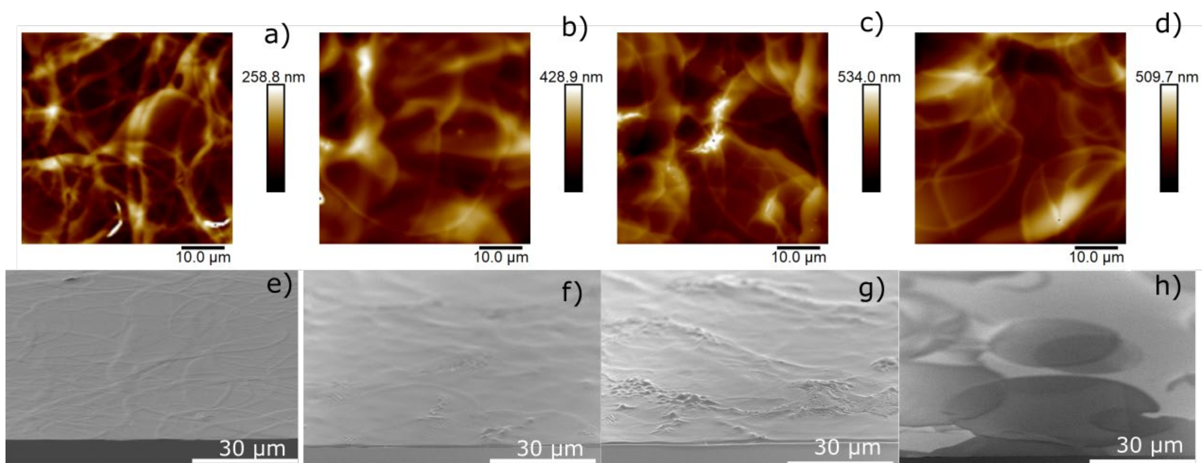

7 *Figure 8: Top: AFM images, bottom: tilted view SEM images of films deposited at 0.75 slm atomizer gas*
8 *flow, 2 scans, a scan speed of 16 mm/s and a scan pitch of 2 mm. a,e) EGDMA, b,f) 2EGDMA, c,g)*
9 *3EGDMA, d,h) PEGDMA.*

1 *Table 3: Root mean squared (RMS) roughness values for films deposited at 0.75 slm atomizer gas flow,*

2 *2 scans a scan speed of 16 mm/s and a scan pitch of 2 mm.*

	EGDMA	*2EGDMA*	*3EGDMA*	*PEGDMA*
RMS roughness (nm)	38	58	78	64
Thickness (nm)	388	725	836	260

3

4 ## Impact of methacrylate precursor structure and mass flow on film composition and stability

5 ### *Characterization of film composition by FT-IR and XPS*

6 Next, we investigate the impact of the precursor mass flow and number of ethylene oxide repeats in
7 the precursor on the film composition using FT-IR and XPS, and we discuss the conditions in which
8 films with the desired composition are formed. Methacrylate precursors can undergo radical chain-
9 like polymerization in a plasma [23], [24]. Typical indications of radical-chain-like polymerization of a
10 methacrylate group are: a decrease in the intensity of the C=C stretching band at 1635 cm^{-1}, a shift of
11 the C=O stretch band from 1720 cm^{-1} to 1750 cm^{-1} indicating the loss of conjugation with the C=C bond,
12 and finally a decrease in the intensity of the $=CH_2$ rocking band at 1320 cm^{-1} [53], [54]. We compare the
13 transmission FT-IR spectra for films deposited from EGDMA, 2EGDMA, 3EGDMA and PEGDMA for a
14 high and a low atomizer gas flow with the spectrum of the unreacted precursor (Figure 9). FT-IR spectra
15 indicate that a part of the C=C bonds are activated by the plasma: compared to the spectra of the liquid
16 precursors, the intensity of the C=C stretching band is overall lower in the spectra of the corresponding
17 plasma deposited films. This effect is amplified when the precursor mass flow is reduced, consistent
18 with a higher energy-per-molecule ratio. The decrease in intensity of the C=C stretching band is
19 accompanied by a shift in position of the C=O stretching band from 1720 cm^{-1} for the precursor to 1750
20 cm^{-1} for the deposited films. The intensity of the $=CH_2$ rocking band is also reduced. All these
21 observations are consistent with radical-chain-like polymerization reactions of the methacrylate
22 groups in the precursor. In contrast, when the deposition is performed without plasma, no
23 polymerization reaction occurs: the intensity of the C=C band is similar as in the precursor spectrum
24 (Supplementary figure 3), demonstrating that the plasma activates the precursor.

25 The C=O stretching band is slightly larger at lower precursor mass flows for all precursors, indicating
26 that oxidation of the precursor by the plasma occurs (see also Supplementary figure 4). The band at
27 1130 cm^{1} in the precursor spectrum, representing stretching vibration of the ether bonds, is still
28 present in the spectra of the deposited films. A broad band is observed containing the symmetric CH_2
29 stretch (2870-2840 cm^{-1}) and the asymmetric CH_2 stretch (2940-2915 cm^{-1}), convoluted with the
30 symmetric CH_3 stretch (2940-2880 cm^{-1}), the asymmetric CH_3 stretch (2975-2950 cm^{-1}) [54]. Together
31 with the CH_2 deformation vibration at 1450 cm^{-1}, this suggests that the CH_2 units are at least partly

1 maintained in the deposited films. A small OH stretching band around 3500 cm^{-1}, not present in the
2 precursor spectrum, also appears in the film spectra.

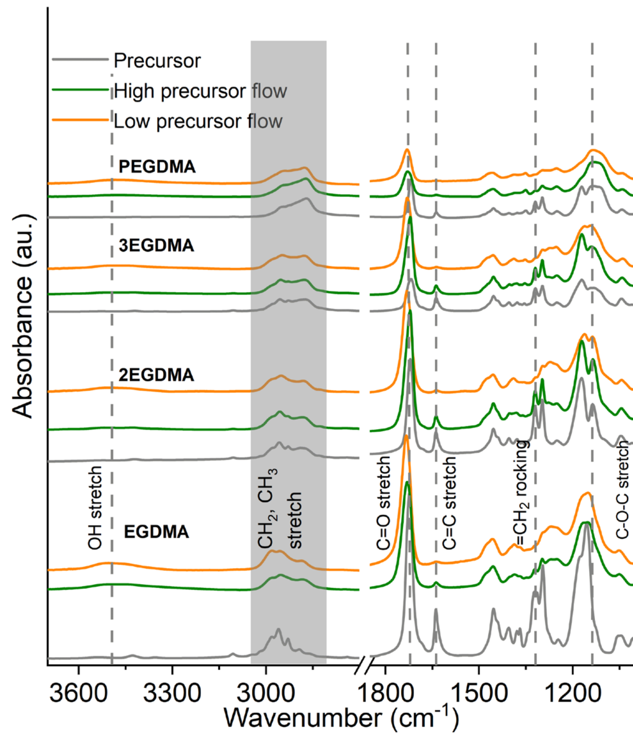

3

4 *Figure 9: Transmission FT-IR spectra of plasma deposited films from EGDMA, 2EGDMA, 3EGDMA and*
5 *PEGDMA at a low and a high precursor mass flow (corresponding to 0.75 and 1.05 slm atomizer gas*
6 *flow respectively), together with the spectrum of the unreacted precursor. All spectra were normalized*
7 *using the integrated CH_2 and CH_3 stretching band.*

8

*Table 4: XPS results of films deposited at 0.75 slm atomizer gas flow: Third column contains atomic percentage (at%) of oxygen in the films. The following columns represent the percentage of the different carbon chemical states, based on the fitting of the C1s peak in the high resolution XPS spectrum. From low to high binding energy representing 4 peaks containing mainly C-C and C-H bonds, C-O bonds, C=O or O-C-O bonds and O-C=O bonds. The last column contains the ratio of the C-O and (O-C=O + C=O) component. XPS was performed on films deposited with 2 scans. The last row contains data of a PEO-SAM reference coating. Values from precursor stoichiometry between brackets. Only O and C were detected. Data for 2EGDVE reproduced from [55] for a film deposited in environment with low air content.*Average number of ethylene oxide repeats*

9

	EO repeats	O at%	CH, C-C %	C-O %	C=O, O-C-O %	O-C=O %	C-O to (O-C=O + C=O) ratio
Binding energy (eV)			284.8	286.4	287.2	288.6	
EGDMA	1	36 (29)	42 (60)	34 (20)	2 (0)	22 (20)	1.4
2EGDMA	2	33 (29)	39 (50)	39 (33)	4 (0)	18 (17)	1.8
3EGDMA	3	32 (30)	38 (43)	41 (43)	6 (0)	15 (14)	1.9
PEGDMA	9*	35 (32)	19 (23)	58 (69)	11 (0)	12 (8)	2.6
2EGDVE [55]	2	41 (27)	19 (25)	65 (75)	11(0)	5(0)	4.1
PEO-SAM [38]	/		17	79	4	0	/

1 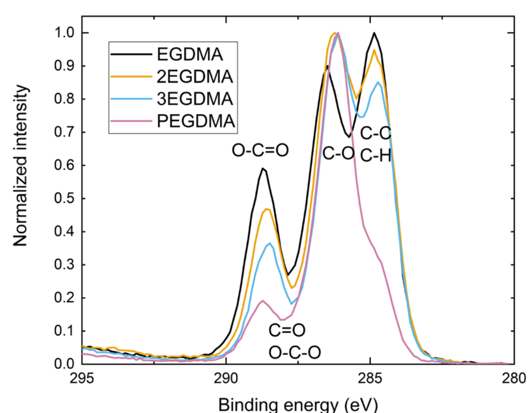

2 *Figure 10: C 1s peak in the high resolution XPS spectrum. Films deposited at 0.75 slm atomizer gas flow.*

3 The composition of the top ~10nm of the deposited films is further analysed by XPS. Figure 10 shows
4 the high-resolution C 1s spectra. The corresponding atomic percentages of the different carbon
5 chemical states after deconvolution are reported in Table 4, together with the atomic percentage of
6 oxygen in the films. The peak fitting can be found in Supplementary figure 6. XPS indicates that the
7 precursor strongly determines the content of C-O bonds in the resulting films: the content of C-O bonds
8 increases when the number of ethylene oxide repeats in the precursor increases, from 34% for EGDMA
9 to 58% for PEGDMA (Table 4). Films deposited from PEGDMA almost reach 60% of C-O bonded carbon,
10 which is often claimed to be necessary for antifouling [56]. The C-O/O-C=O ratio of the films increases
11 with increasing ethylene oxide repeats (1.4 vs 2.6 for EGDMA and PEGDMA respectively, Table 4). This
12 suggests that we deposit a poly(ethylene oxide) ester in which the ethylene oxide to ester ratio is
13 controlled by the precursor composition. We therefore refer to the films as PEO-like films.
14 The content of C-O bonded carbon in the films deposited from EGDMA and 2EGDMA is higher than
15 the C-O content in the precursor (34% versus 20% for EGDMA, and 39% versus 33% for 2EGDMA). This

potentially indicates that a part of the C-O bonded carbon consists of C-OH bonds, in agreement with the appearance of an OH stretch in the FT-IR spectra (Figure 9). For PEGDMA the C-O component is decreased with respect to the precursor (58% vs 69% respectively), which could indicate that a fraction of the C-O bonds is fragmented or oxidized by the plasma.

Finally, there is a decrease in C-C and C-H content with respect to the precursor, except when deposition is performed with PEGDMA. This can potentially be explained by oxygen binding to an activated C radical site, leading to formation of C=O, C-OH or O-C=O. This agrees with the increase in O-content (36 vs 29 %) and C-O content (34 vs 20%) in the coatings with respect to the precursor for EGDMA (Table 4). In literature, oxygen uptake is common for plasma deposition with open air processing, meaning that the films are exposed to air during and after deposition [30].

Impact of C=C bond conversion on film stability in water

For practical applications it is crucial that the films are stable in water. Therefore, we investigate how the precursors and deposition conditions (e.g. precursor mass flow) affect the C=C bond conversion and as such the film stability in water. A high C=C bond conversion is expected to result in a good cross-linking and a high film stability in water. The C=C bond conversion ϕ is defined as:

$$\phi = 1 - \frac{I_{C=C,film}/I_{CH,film}}{I_{C=C,precursor}/I_{CH,precursor}} \qquad (9)$$

with $I_{C=C,precursor}$ and $I_{CH,precursor}$ respectively the integrated C=C and CH band intensity in the FT-IR spectrum of the precursor and $I_{C=C,film}$ and $I_{CH,film}$ respectively the integrated C-C and CH band intensity in the FT-IR spectrum of the deposited film. ϕ decreases with increasing atomizer gas flow for all methacrylate precursors (Figure 11a), which can be explained by a higher energy-per-molecule ratio at lower atomizer gas flows in agreement with literature [24].

For EGDMA, the C=C bond conversion is above 90% for all tested atomizer gas flows. This is consistent with the low material balance for EGDMA (5%, Figure 4b) and impact of the droplets on the substrate: for the most volatile EGDMA precursor, only a small fraction of the injected precursor reaches the substrate due to fast evaporation of droplets during transport and evaporation from the substrate after impaction. Moreover, droplets that reach the substrate spread out easily due to the low viscosity. Both effects result in an effective interaction of the plasma with the precursor and a high energy-per-molecule, consistent with the high C=C bond conversion.

For 2EGDMA and 3EGDMA the C=C bond conversion during deposition is lower as compared to EGDMA, in conditions with higher atomizer gas flows. For example, the C=C bond conversion is only 55% for the atomizer gas flow of 1.05 slm. This lower C=C bond conversion despite the lower precursor mass flow could be explained by the higher η (~17% and ~23% for 2EGDMA and 3EGDMA respectively, Figure 4b) resulting in a lower energy-per-molecule at the substrate, and by the higher viscosity, reducing the spreading of the precursor on the substrate (Figure 7b).

For PEGDMA, the C=C bond conversion values are higher than for 2EGDMA and 3EGDMA, even at high atomizer gas flows. This seems unexpected as the lower surface-to-volume ratio of the droplets after impact and spreading on the surface could limit the interaction between the plasma and the precursor. The higher C=C bond conversion value could be explained by the much lower precursor mass flow of PEGDMA (Figure 3a), whereas the material balance is similar for 3EGDMA and PEGDMA (Figure 4b): a lower number density of droplets that reach the surface could result in higher energy-per-molecule at the substrate and higher degree of C=C bond conversion.

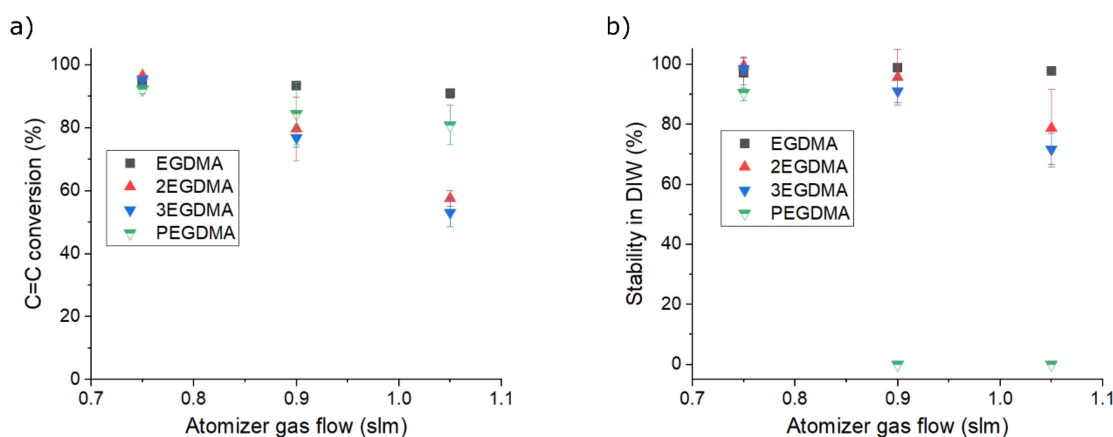

Figure 11: a) C=C bond conversion as a function of the atomizer gas flow. b) Stability of the films when soaking in deionized water in function of the atomizer gas flow. The error bars represent the standard deviation on 3 separately deposited samples.

The stability of the films in water is defined as the percentage of the intensity of the integrated bands containing CH_2 and CH_3 symmetric and asymmetric stretching in the FT-IR spectrum that remains present after soaking the films in water for 10 minutes. The stability of the films deposited at the lowest atomizer gas flow of 0.75 slm is close to 100% for all methacrylate precursors, in agreement with the high C=C bond conversion values (Figure 11b). The stability decreases at higher atomizer gas flows for films deposited from 2EGDMA (79% at 1.05 slm) and 3EGDMA (72% at 1.05 slm). This agrees with a decrease in C=C bond conversion. For PEGDMA the films are only stable at 0.75 slm atomizer gas flow. At higher precursor gas flows, the films delaminate from the substrate, making it impossible to determine the stability. The delamination cannot directly be linked to the FT-IR results but could be explained by a poor adhesion to the substrate, which merits further investigation but is beyond the scope of this work.

1 ## Antifouling properties

2 Finally, we investigate the antifouling properties of the plasma deposited PEO-like films. A PEO-like
3 antifouling coating should prevent the non-specific binding of proteins from a solution to the
4 surface [57]. This was tested by measuring the binding of a fluorescently labelled anti-mouse IgG
5 antibodies. The antifouling performance of the plasma deposited PEO film is compared with three
6 reference samples: a PEO-SAM with high concentration of C-O bonded carbon (low fouling) [58], an
7 SiO_2 substrate with thermal oxide (high fouling) and an azide-SAM (high fouling).
8 Films deposited from EGDMA, 2EGDMA and 3EGDMA significantly reduce the fouling with respect to
9 the SiO_2 substrate and the azide-SAM (Figure 12). Films deposited from PEGDMA strongly reduced
10 fouling compared to films from EGDMA, 2EGDMA and 3EGDMA, but still show higher fouling than the
11 PEO-SAM reference. The degree of fouling agrees with the C-O/(C=O + O-C=O) ratio from XPS (Table
12 4): a high degree of fouling corresponds to a low C-O/(C=O + O-C=O) ratio (1.4 for EGDMA), a low
13 degree of fouling can be expected for a high C-O/(C=O + O-C=O) ratio (2.6 for PEGDMA).

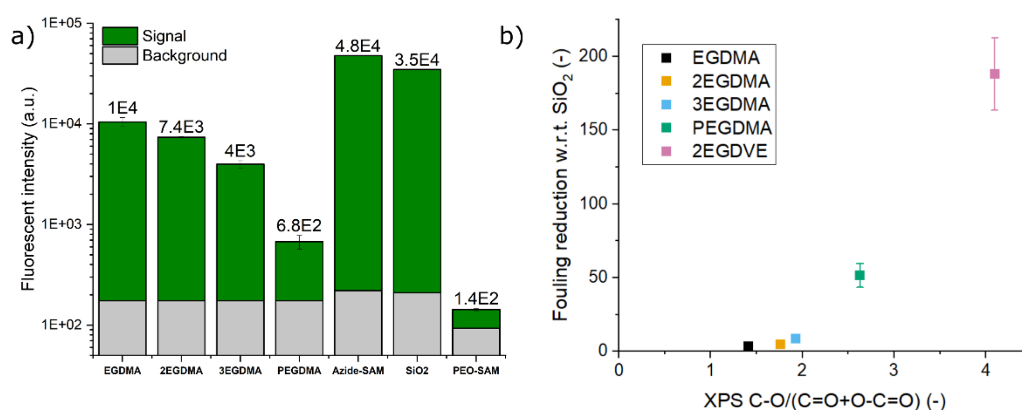

14

15 *Figure 12: a) Fluorescent intensity, plotted on a logarithmic scale, for the deposited films and reference samples after exposure*
16 *to the fluorescent antibody solution. Error bars are standard deviation based on 6 measurements on 3 different samples. All*
17 *films were deposited at 0.75 slm atomizer gas flow. b): Fouling reduction factor with respect to untreated SiO2, as a function*
18 *of the C-O/(C=O+O-C=O) ratio from XPS. Fouling reduction factor obtained by dividing fluorescent intensity of the SiO_2*
19 *reference by the value for the respective precursor. Datapoint for 2EGDVE adapted from [55] for film deposited in environment*
20 *with low air content.*

21 ## Comparison with 2EGDVE precursor

22 In previous work, we deposited antifouling thin films from di(ethylene glycol) divinyl ether (2EGDVE)
23 [55], which has vinyl instead of methacrylate polymerizable groups. It is interesting to study the impact
24 of the polymerizable group on the cross-linking and antifouling properties. The plasma polymerization
25 of 2EGDVE is inhibited in presence of air [55]. Therefore, it is necessary to perform depositions in an

environment with low air content to obtain water stable coatings from 2EGDVE, which is less convenient for mass manufacturing. This is in contrast with films deposited from the methacrylate precursors investigated in this paper, for which the film stability in water is governed by the C=C bond conversion. Films from 2EGDVE exhibit better antifouling properties compared to PEGDMA (Figure 12b), despite 2EGDVE having only 2 ethylene oxide repeats in the precursor structure, compared to 9 for PEGDMA. This can be attributed to the ester functionalities in the methacrylate precursors, which are preserved during plasma deposition, resulting in a poly(ethylene oxide)-ester film. These ester functionalities negatively impact the antifouling properties. Consequently, the ethylene oxide to ester ratio is higher for films deposited from 2EGDVE compared to PEGDMA (4.1 vs 2.6 for 2EGDVE and PEGDMA respectively). This demonstrates the trade-off between cross-linking and antifouling properties: methacrylate precursors are easier to cross-link, but inherently incorporate ester functionalities in the film which adversely affect the antifouling properties.

Conclusion and outlook

Aerosol-assisted plasma deposition using a CAPjet allows the deposition of a wide range of coatings for different applications such as antifouling coatings, which remain of high interest for biomedical applications. We investigated the impact of the physical precursor properties such as vapor pressure and viscosity on the deposition of PEO-like antifouling films with CAPjet. The aerosol injection of the precursor allows us to explore precursors with many ethylene oxide repeats, 9 repeats for PEGDMA. Increasing the number of ethylene oxide repeats enables us to increase the C-O content in the deposited films, which improves the antifouling properties of the films. Films deposited from the PEGDMA precursor yield better antifouling properties compared to films deposited from EGDMA, in agreement with the higher C-O content of the film (58% versus 34%) and relatively lower content of C-C and O-C=O bonds in the precursor and the final film. The precursor vapor pressure and viscosity strongly affect the material balance and resulting film composition and morphology. We propose the following mechanism to explain these observations. The more volatile methacrylate precursors with low number of ethylene oxide repeats evaporate more during transport to the substrate, resulting in fewer droplets that reach the substrate. More evaporation occurs also after impaction of the droplets on the substrate. This high degree of evaporation can explain the low material balance (η) when using the most volatile precursors. It leads to thinner films with more converted C=C bonds, consistent with a higher energy-per-molecule at the substrate. The less volatile and more viscous methacrylate precursors evaporate less during transport and on the substrate, leading to a higher material balance. To maximize the material balance of the aerosol assisted plasma deposition process it is therefore recommended to use precursors with a low volatility. What remains unclear is the formation of rings after impact of the droplets on the substrate and the role of the plasma during this process. The degree

of cross-linking in the deposited films and the stability of the films in water can be additionally tuned by the precursor mass flow of methacrylate precursors. Decreasing the precursor mass flow increases the degree of C=C bond conversion and crosslinking, consistent with higher energy-per-molecule and radical-chain like polymerization of the methacrylate groups.

This work demonstrates that both chemical and physical precursor properties affect aerosol-assisted deposition process of poly(ethylene oxide)-like films, as they affect the composition, morphology and antifouling properties of the resulting films. Better understanding of the mechanisms during aerosol-assisted plasma deposition facilitates the development and design of adequate precursors and enable well-controlled modulation of the composition and properties of a wide range of films for various applications.

Conflicts of interest

Bernard Nisol is an employee of Molecular Plasma Group.

Acknowledgements

T. Dekoster acknowledges the financial support from the Flemish Science Foundation (FWO) under project number 1SD6623N. The authors thank Ilse Hoflijk and Thierry Conard from imec for the XPS measurements and an anonymous referee for the valuable feedback.

References

[1] F. Palumbo, C. Lo Porto, F. Fracassi, and P. Favia, “Recent Advancements in the Use of Aerosol-Assisted Atmospheric Pressure Plasma Deposition,” *Coatings*, vol. 10, no. 5, p. 440, Apr. 2020, doi: 10.3390/coatings10050440.

[2] M. Kehrer, A. Rottensteiner, W. Hartl, J. Duchoslav, S. Thomas, and D. Stifter, “Cold atmospheric pressure plasma treatment for adhesion improvement on polypropylene surfaces,” *Surface and Coatings Technology*, vol. 403, p. 126389, Dec. 2020, doi: 10.1016/j.surfcoat.2020.126389.

[3] Z. Jeckell *et al.*, “Silicon Dioxide Deposited Using Atmospheric Pressure Plasma Chemical Vapor Deposition for Improved Adhesion and Water Intrusion Resistance for Lightweight Manufacturing,” *Surfaces and Interfaces*, vol. 23, p. 100989, Apr. 2021, doi: 10.1016/j.surfin.2021.100989.

[4] G. Buyle, “Nanoscale finishing of textiles via plasma treatment,” *Materials Technology*, vol. 24, no. 1, pp. 46–51, Mar. 2009, doi: 10.1179/175355509X417954.

[5] Md. M. Hossain, Q. H. Trinh, D. B. Nguyen, M. S. P. Sudhakaran, and Y. S. Mok, “Robust hydrophobic coating on glass surface by an atmospheric-pressure plasma jet for plasma-

1 polymerisation of hexamethyldisiloxane conjugated with (3-aminopropyl) triethoxysilane,"
2 *Surface Engineering*, vol. 35, no. 5, pp. 466–475, May 2019, doi:
3 10.1080/02670844.2018.1524037.
4 [6] S. Lowe, N. M. O'Brien-Simpson, and L. A. Connal, "Antibiofouling polymer interfaces:
5 poly(ethylene glycol) and other promising candidates," *Polymer Chemistry*, vol. 6, no. 2, pp. 198–
6 212, 2015, doi: 10.1039/C4PY01356E.
7 [7] S.-W. Lee and P. E. Laibinis, "Protein-resistant coatings for glass and metal oxide surfaces derived
8 from oligo(ethylene glycol)-terminated alkyltrichlorosilanes," *Biomaterials*, vol. 19, no. 18, pp.
9 1669–1675, Sep. 1998, doi: 10.1016/S0142-9612(98)00044-1.
10 [8] M. Cerruti, S. Fissolo, C. Carraro, C. Ricciardi, A. Majumdar, and R. Maboudian, "Poly(ethylene
11 glycol) Monolayer Formation and Stability on Gold and Silicon Nitride Substrates," *Langmuir*, vol.
12 24, no. 19, pp. 10646–10653, Oct. 2008, doi: 10.1021/la801357v.
13 [9] A. Papra, N. Gadegaard, and N. B. Larsen, "Characterization of Ultrathin Poly(ethylene glycol)
14 Monolayers on Silicon Substrates," *Langmuir*, vol. 17, no. 5, pp. 1457–1460, Mar. 2001, doi:
15 10.1021/la000609d.
16 [10] W. Feng, S. Zhu, K. Ishihara, and J. L. Brash, "Protein resistant surfaces: Comparison of acrylate
17 graft polymers bearing oligo-ethylene oxide and phosphorylcholine side chains," *Biointerphases*,
18 vol. 1, no. 1, pp. 50–60, Mar. 2006, doi: 10.1116/1.2187495.
19 [11] C. Rodriguez-Emmenegger, M. Houska, A. B. Alles, and E. Brynda, "Surfaces Resistant to Fouling
20 from Biological Fluids: Towards Bioactive Surfaces for Real Applications," *Macromolecular*
21 *Bioscience*, vol. 12, no. 10, pp. 1413–1422, Oct. 2012, doi: 10.1002/mabi.201200171.
22 [12] S. Tugulu and H.-A. Klok, "Stability and Nonfouling Properties of Poly(poly(ethylene glycol)
23 methacrylate) Brushes under Cell Culture Conditions," *Biomacromolecules*, vol. 9, no. 3, pp. 906–
24 912, Mar. 2008, doi: 10.1021/bm701293g.
25 [13] H. Ma, M. Wells, T. P. Beebe, and A. Chilkoti, "Surface-Initiated Atom Transfer Radical
26 Polymerization of Oligo(ethylene glycol) Methyl Methacrylate from a Mixed Self-Assembled
27 Monolayer on Gold," *Advanced Functional Materials*, vol. 16, no. 5, pp. 640–648, Mar. 2006, doi:
28 10.1002/adfm.200500426.
29 [14] J. Sung, D. G. Lee, S. Lee, J. Park, and H. W. Jung, "Crosslinking Dynamics and Gelation
30 Characteristics of Photo- and Thermally Polymerized Poly(Ethylene Glycol) Hydrogels," *Materials*,
31 vol. 13, no. 15, p. 3277, Jul. 2020, doi: 10.3390/ma13153277.
32 [15] J. W. Hwang, S. M. Noh, B. Kim, and H. W. Jung, "Gelation and crosslinking characteristics of
33 photopolymerized poly(ethylene glycol) hydrogels," *J. Appl. Polym. Sci.*, vol. 132, no. 22, Jun.
34 2015, doi: 10.1002/app.41939.

1 [16] F. Palumbo, P. Favia, and M. Vulpio, “RF Plasma Deposition of PEO-Like Films: Diagnostics and
2 Process Control,” *Plasmas and Polymers*, p. 12, 2001, doi:
3 https://doi.org/10.1023/A:1013144612953.
4 [17] E. E. Johnston, J. D. Bryers, and B. D. Ratner, “Plasma Deposition and Surface Characterization of
5 Oligoglyme, Dioxane, and Crown Ether Nonfouling Films,” *Langmuir*, vol. 21, no. 3, pp. 870–881,
6 Feb. 2005, doi: 10.1021/la036274s.
7 [18] G. Da Ponte, E. Sardella, F. Fanelli, R. d’Agostino, R. Gristina, and P. Favia, “Plasma Deposition of
8 PEO-Like Coatings with Aerosol-Assisted Dielectric Barrier Discharges,” *Plasma Processes and*
9 *Polymers*, vol. 9, no. 11–12, pp. 1176–1183, Dec. 2012, doi: 10.1002/ppap.201100201.
10 [19] B. Nisol *et al.*, “Atmospheric plasma synthesized PEG coatings: non-fouling biomaterials showing
11 protein and cell repulsion,” *Surface and Coatings Technology*, vol. 252, pp. 126–133, Aug. 2014,
12 doi: 10.1016/j.surfcoat.2014.04.056.
13 [20] “Sigma Aldrich product database,” Product numbers: EGDMA: 335681, 2EGDMA: 409006,
14 3EGDMA: 261548. Accessed: Feb. 16, 2025. [Online]. Available:
15 https://www.sigmaaldrich.com/BE/en
16 [21] G. Morand, P. Chevallier, M. Tatoulian, and D. Mantovani, “Aerosol-assisted open-air plasma
17 deposition of acrylate-based composite coatings: Molecule release control through precursor
18 selection,” *Plasma Processes & Polymers*, vol. 19, no. 7, p. 2100252, Jul. 2022, doi:
19 10.1002/ppap.202100252.
20 [22] V. Jalaber *et al.*, “Atmospheric Aerosol Assisted Pulsed Plasma Polymerization: An
21 Environmentally Friendly Technique for Tunable Catechol-Bearing Thin Films,” *Frontiers in*
22 *Chemistry*, vol. 7, Apr. 2019, doi: 10.3389/fchem.2019.00183.
23 [23] C. Rendon-Piedrahita *et al.*, “Effect of crosslinker on the wettability and mechanical properties of
24 hydrophobic coatings deposited via atmospheric pressure plasma,” *Plasma Processes &*
25 *Polymers*, vol. 19, no. 8, p. 2200023, Aug. 2022, doi: 10.1002/ppap.202200023.
26 [24] J. Bardon *et al.*, “Mechanical properties of thin plasma polymer coatings from hexanediol
27 dimethacrylate and relations with their chemical properties,” *Surface and Coatings Technology*,
28 vol. 358, pp. 320–330, Jan. 2019, doi: 10.1016/j.surfcoat.2018.10.064.
29 [25] P. A. F. Herbert, L. O’Neill, and J. Jaroszyńska-Wolińska, “Soft Plasma Polymerization of Gas State
30 Precursors from an Atmospheric Pressure Corona Plasma Discharge,” *Chem. Mater.*, vol. 21, no.
31 19, pp. 4401–4407, Oct. 2009, doi: 10.1021/cm900816e.
32 [26] H. Yasuda, “Glow discharge polymerization,” *J. Polym. Sci. Macromol. Rev.*, vol. 16, no. 1, pp. 199–
33 293, Jan. 1981, doi: 10.1002/pol.1981.230160104.

1 [27] J. Petersen *et al.*, “Nano-ordered thin films achieved by soft atmospheric plasma polymerization,”
2 *RSC Advances*, vol. 3, no. 13, p. 4416, 2013, doi: 10.1039/c2ra21833j.
3 [28] A. Dembele, M. Rahman, I. Reid, B. Twomey, J. M. D. MacElroy, and D. P. Dowling, “Deposition of
4 Hybrid Organic–Inorganic Composite Coatings Using an Atmospheric Plasma Jet System,” *J.*
5 *Nanosci. Nanotech.*, vol. 11, no. 10, pp. 8730–8737, Oct. 2011, doi: 10.1166/jnn.2011.3459.
6 [29] P. J. Bruggeman *et al.*, “Plasma–liquid interactions: a review and roadmap,” *Plasma Sources*
7 *Science and Technology*, vol. 25, no. 5, p. 053002, Sep. 2016, doi: 10.1088/0963-
8 0252/25/5/053002.
9 [30] J. Friedrich, “Mechanisms of Plasma Polymerization - Reviewed from a Chemical Point of View,”
10 *Plasma Processes and Polymers*, vol. 8, no. 9, pp. 783–802, Sep. 2011, doi:
11 10.1002/ppap.201100038.
12 [31] A. Batan *et al.*, “The Impact of Double Bonds in the APPECVD of Acrylate-Like Precursors,” *Plasma*
13 *Processes and Polymers*, vol. 10, no. 10, pp. 857–863, Oct. 2013, doi: 10.1002/ppap.201300054.
14 [32] “Sigma Aldrich specification sheet.” Accessed: Sep. 16, 2024. [Online]. Available:
15 https://www.sigmaaldrich.com/BE/en/product/aldrich/335681
16 [33] O. L. I. Brown, “The Clausius-Clapeyron equation,” *J. Chem. Educ.*, vol. 28, no. 8, p. 428, Aug.
17 1951, doi: 10.1021/ed028p428.
18 [34] “Chemical book.” Accessed: Dec. 02, 2025. [Online]. Available:
19 https://www.chemicalbook.com/ProductMSDSDetailCB8146599_EN.htm
20 [35] V. Piacente, D. Fontana, and P. Scardala, “Enthalpies of Vaporization of a Homologous Series of
21 n-Alkanes Determined from Vapor Pressure Measurements,” *J. Chem. Eng. Data*, vol. 39, no. 2,
22 pp. 231–237, Apr. 1994, doi: 10.1021/je00014a009.
23 [36] J. Borek-Donten *et al.*, “The industrial process for virucidal plasma coatings on textiles: From idea
24 to upscaling,” *Plasma Processes & Polymers*, vol. 19, no. 10, p. 2100249, Oct. 2022, doi:
25 10.1002/ppap.202100249.
26 [37] D. A. Shirley, “High-Resolution X-Ray Photoemission Spectrum of the Valence Bands of Gold,”
27 *Phys. Rev. B*, vol. 5, no. 12, pp. 4709–4714, Jun. 1972, doi: 10.1103/PhysRevB.5.4709.
28 [38] K. Jans, “Het gebruik van poly-(ethyleenglycol) gemodificeerde trichloorsilanen voor de opbouw
29 van proteïneresistente oxide-oppervlakken,” PhD thesis, KU Leuven, 2004.
30 [39] R. Vos *et al.*, “Chemical Vapor Deposition of Azidoalkylsilane Monolayer Films,” *Langmuir*, vol.
31 34, no. 4, pp. 1400–1409, Jan. 2018, doi: 10.1021/acs.langmuir.7b04011.
32 [40] W. H. Finlay, “Particle size changes due to evaporation or condensation,” in *The Mechanics of*
33 *Inhaled Pharmaceutical Aerosols*, Elsevier, 2019, pp. 53–101. doi: 10.1016/B978-0-08-102749-
34 3.00004-X.

[41] T.-C. Le and C.-J. Tsai, "Inertial Impaction Technique for the Classification of Particulate Matters and Nanoparticles: A Review," *KONA*, vol. 38, no. 0, pp. 42–63, Jan. 2021, doi: 10.14356/kona.2021004.

[42] L. Cacot, G. Carnide, M. L. Kahn, R. Clergereaux, N. Naudé, and L. Stafford, "Kinetics driving thin-film deposition in dielectric barrier discharges using a direct liquid injector operated in a pulsed regime," *J. Phys. D: Appl. Phys.*, vol. 55, no. 47, p. 475202, Nov. 2022, doi: 10.1088/1361-6463/ac94de.

[43] W. Gu, P. Cheng, and M. Tang, "Compilation and evaluation of gas phase diffusion coefficients of halogenated organic compounds," *R. Soc. open sci.*, vol. 5, no. 7, p. 171936, Jul. 2018, doi: 10.1098/rsos.171936.

[44] J. Q. Feng, L.-S. Go, J. Calubayan, and R. Tomaska, "Working Mechanism and Behavior of Collison Nebulizer," *Aerosol Sci Eng*, vol. 5, no. 3, pp. 285–291, Sep. 2021, doi: 10.1007/s41810-021-00102-9.

[45] K. R. May, "The collison nebulizer: Description, performance and application," *Journal of Aerosol Science*, vol. 4, no. 3, pp. 235–243, May 1973, doi: 10.1016/0021-8502(73)90006-2.

[46] S. Sazhin, *Droplets and Sprays*. London: Springer London, 2014. doi: 10.1007/978-1-4471-6386-2.

[47] S. Tonini and G. E. Cossali, "An analytical model of liquid drop evaporation in gaseous environment," *International Journal of Thermal Sciences*, vol. 57, pp. 45–53, Jul. 2012, doi: 10.1016/j.ijthermalsci.2012.01.017.

[48] W. Li and E. J. Davis, "Aerosol Evaporation in the Transition Regime," *Aerosol Science and Technology*, vol. 25, no. 1, pp. 11–21, Jan. 1996, doi: 10.1080/02786829608965375, note that there is a factor M missing in eqs. 1 and 2.

[49] R. Mauchauffé, M. Moreno-Couranjou, N. D. Boscher, A.-S. Duwez, and P. Choquet, "Liquid-Assisted Plasma-Enhanced Chemical Vapor Deposition of Catechol and Quinone-Functionalized Coatings: Insights into the Surface Chemistry and Morphology," *Plasma Process. Polym.*, vol. 13, no. 8, pp. 843–856, Aug. 2016, doi: 10.1002/ppap.201600002.

[50] M. Qin, C. Tang, S. Tong, P. Zhang, and Z. Huang, "On the role of liquid viscosity in affecting droplet spreading on a smooth solid surface," *International Journal of Multiphase Flow*, vol. 117, pp. 53–63, Aug. 2019, doi: 10.1016/j.ijmultiphaseflow.2019.05.002.

[51] D. Mariotti, J. Patel, V. Švrček, and P. Maguire, "Plasma–Liquid Interactions at Atmospheric Pressure for Nanomaterials Synthesis and Surface Engineering," *Plasma Processes & Polymers*, vol. 9, no. 11–12, pp. 1074–1085, Dec. 2012, doi: 10.1002/ppap.201200007.

[52] I. Azevedo Gonçalves, D. Abessolo Ondo, N. D. Boscher, and R. Quintana, “Free-Radical Polymerization of Liquid Hydroxyethyl Methacrylate Layers Using Nanosecond Plasma Pulses,” *Plasma Processes & Polymers*, vol. 22, no. 1, p. 2400224, Jan. 2025, doi: 10.1002/ppap.202400224.

[53] S. Bäckström *et al.*, “Tailoring Properties of Biocompatible PEG-DMA Hydrogels with UV Light,” *MSA*, vol. 03, no. 06, pp. 425–431, 2012, doi: 10.4236/msa.2012.36060.

[54] G. Socrates, *Infrared and Raman Characteristic Group Frequencies: Tables and Charts, 3rd Edition*, 3rd ed. John Wiley & Sons Ltd, 2001.

[55] T. Dekoster *et al.*, “Impact of open-air processing on atmospheric pressure plasma deposition of poly(ethylene oxide) coatings for antifouling applications,” *Plasma Processes & Polymers*, vol. 21, no. 7, p. 2400019, Jul. 2024, doi: 10.1002/ppap.202400019.

[56] C. P. Stallard, P. Solar, H. Biederman, and D. P. Dowling, “Deposition of Non-Fouling PEO-Like Coatings Using a Low Temperature Atmospheric Pressure Plasma Jet,” *Plasma Processes and Polymers*, vol. 13, no. 2, pp. 241–252, Feb. 2016, doi: 10.1002/ppap.201500034.

[57] R. Konradi, C. Acikgoz, and M. Textor, “Polyoxazolines for Nonfouling Surface Coatings - A Direct Comparison to the Gold Standard PEG,” *Macromolecular Rapid Communications*, vol. 33, no. 19, pp. 1663–1676, Oct. 2012, doi: 10.1002/marc.201200422.

[58] R. De Palma, “Surface engineering : immunosensor interfaces, magnetic biosensors and magnetic nanoparticles,” PhD thesis, KU Leuven, 2007. [Online]. Available: https://imec-publications.be/handle/20.500.12860/11969